AGU100 ADVANCING EARTH AND SPACE SCIENCE

JGR

Journal of Geophysical Research: Space Physics

RESEARCH ARTICLE

10.1029/2018JA025648

Ionospheric Specification and Space Weather Forecasting With an HF Beacon Network in the Peruvian Sector

D. L. Hysell[1], Y. Baumgarten[2], M. A. Milla[3], A. Valdez[3], and K. Kuyeng[3]

[1]Earth and Atmospheric Sciences, Cornell University, Ithaca, NY, USA, [2]Mechanical and Aerospace Engineering, Cornell University, Ithaca, NY, USA, [3]Jicamarca Radio Observatory, Lima, Peru

Key Points:

- An expanding network of HF beacon transmitters and receivers is being deployed in Peru for purposes of ionospheric specification
- Pseudorange and Doppler shift data from network observed at two frequencies are inverted to give a regional specification of *F* region
- In a campaign in January 2018 the beacon data help explain why ESF occurred on one evening but not the next

Correspondence to:
D. L. Hysell,
dlh37@cornell.edu

Citation:
Hysell, D. L., Baumgarten, Y., Milla, M. A., Valdez, A., & Kuyeng, K. (2018). Ionospheric specification and space weather forecasting with an HF beacon network in the Peruvian sector. *Journal of Geophysical Research: Space Physics*, *123*, 6851–6864. https://doi.org/10.1029/2018JA025648

Received 6 MAY 2018
Accepted 25 JUL 2018
Accepted article online 14 AUG 2018
Published online 21 AUG 2018

Abstract A network of high-frequency (HF) transmitters and receivers used for ionospheric specification is being installed in Peru. The HF transmitters employ multiple frequencies and binary phase coding with pseudorandom noise, and the observables provided by the receivers include group delay, Doppler shift, amplitude, bearing (from interferometry), and polarization. Statistical inverse methods are used to estimate *F* region density in a volume from the data regionally. The method incorporates raytracing based on the principles of Hamiltonian optics in the forward model and involves an ionospheric parametrization in terms of Chapman functions in the vertical and bicubic B-spline interpolation in the horizontal. Regularization is employed to minimize the global curvature of the reconstructions. HF beacon data for two nights in January 2018 are presented. We use the reconstructions to investigate why plasma irregularities associated with equatorial spread *F* formed on one occasion and not the other. The data indicate that the background ionospheric flow is not simply frozen in, that is, that longitude and local time variations cannot be equated, even at regional scales. This has ramifications for equatorial spread *F* forecasting strategies that assume equivalence.

1. Introduction

The most important space weather agent at low geomagnetic latitudes is a class of convective plasma instabilities operating in the postsunset *F* region ionosphere. The instabilities produce plasma density irregularities that cause range and frequency spreading in ionograms, a phenomenon known as equatorial spread *F* (ESF; Booker & Wells, 1938). The irregularities also cause diffraction and scattering in radio signals, posing a hazard to ground- and space-based radio communication, navigation, and imaging systems (see Kelley et al., 2011; Woodman, 2009, for recent reviews). In radar backscatter, the irregularities appear as spectacular plumes ascending into the topside.

The dominant instabilities in ESF are variants of the collisional interchange instability, which occurs in plasmas where currents driven by gravity, a background electric field, and neutral winds flow in regions where the Pedersen conductivity is finite and inhomogeneous such as the postsunset bottomside *F* region (Zargham & Seyler, 1987). By definition, inertia is negligible in the collisional interchange instability, which therefore does not produce inertial range turbulence. Instead, instability tends to form steepened structures, which occupy a broad continuum of spatial scale sizes (Costa & Kelley, 1978). The broadband aspect of the phenomenon makes it disruptive to a wide range of systems.

The collisional interchange instability occurs frequently in the equatorial zone and is influenced by but not dependent on solar and geomagnetic conditions. It has been studied analytically and with two- and three-dimensional numerical simulations for decades (e.g., Huba et al., 2008; Keskinen et al., 1980; Ossakow, 1981; Retterer, 2010; Yokoyama et al., 2014; Zargham & Seyler, 1987). While the most important characteristics observed experimentally have been reproduced in simulation, the phenomenon has so far resisted numerical forecasting.

A series of studies combining a 3-D numerical simulation code with comprehensive ionospheric observations from the Jicamarca Radio Observatory have shown some forecasting promise (Hysell, Jafari, et al., 2014; Hysell, Milla, et al., 2014; Hysell et al., 2015). The simulation is initialized and forced so as to be consistent with plasma density and drift profiles measured using the incoherent scatter technique at Jicamarca starting at sunset. Irregularities produced by the simulation can be compared with those observed by Jicamarca using coherent scatter techniques to assess forecast skill. A novel feature of the simulation is that it encompasses vertical

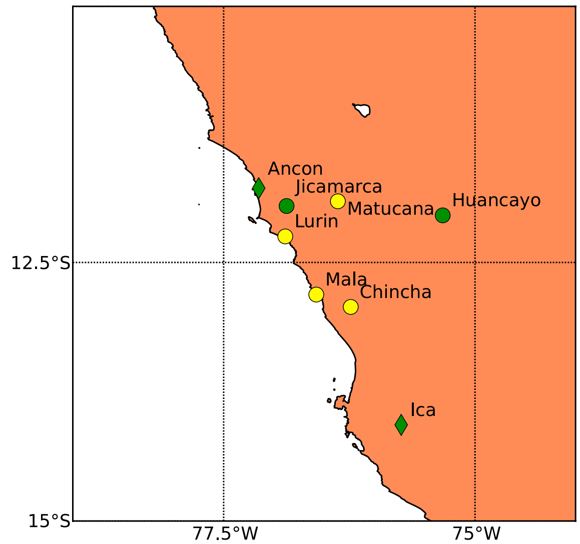

Figure 1. Map of current (green) and planned (yellow) high-frequency beacon sites. Diamonds are transmit-only sites.

currents in the *F* region driven by zonal winds. These currents are strong around sunset and can be the dominant driver for a variant of collisional interchange instability (Hysell & Kudeki, 2004). Another novel feature of the simulation code is that it solves for the electrostatic potentially fully in three dimensions. This is necessary for recovering realistic flows and currents in the postsunset bottomside and valley regions (Aveiro & Hysell, 2012).

The aforementioned simulation has not produced *false alarms* or predictions of irregularities that were not actually observed. It has produced some *missed detections*, failing to predict some radar plumes and topside irregularities that were observed. A shortcoming of the forecast strategy that could be responsible stems from the inability of the Jicamarca radar to observe conditions other than those immediately overhead. The strategy extrapolates Jicamarca observations using a combination of empirical models and by equating local time and longitudinal variations in some model parameters. The approach appears to be limiting.

We have therefore expanded the experimental zone in latitude and longitude with the deployment of a regional network of high-frequency (HF) beacons. Autonomous HF transmitters and receivers have been deployed to four sites in Western Peru. Continuous wave signals are transmitted at two frequencies using binary phase coding and pseudorandom noise (PRN) codes. Reception is performed with multiple antennas. The observables are signal amplitude, group delay or pseudorange, Doppler shift or optical path length, bearing (using interferometry), and polarization. Statistical inverse methods can be used to estimate the ionospheric electron density regionally and to assess conditions leading to instability and ESF. The goal is to augment the ongoing ESF forecasting effort at Jicamarca using incoherent scatter radar (ISR) and beacon data captured together in campaigns.

Below, we describe the beacon network and the data processing, present some campaign data taken in January of 2018, and assess the possible contribution to ESF forecasting.

2. Beacon Network

See Figure 1 for a map of current and planned HF beacon station sites. The beacon network presently consists of one transmitting station at Ancon (11°46′37′′S, 77°09′1′′W, 51 m above sea level [asl]), one transmitting station at Ica (14°4′ 24.6′′S, 75°44′08.02′′W, 402 m asl), one receiving station at Jicamarca with dual receivers (11°57′5.8′′S, 76°52′27′′W, 510 m asl), and one receiving station in Huancayo with dual receivers (12°02′30′′S, 75°19′15′′W, 3,315 m asl). While it is possible to collocate transmitting and receiving stations, we have yet to do so.

Each beacon transmitter is actually two transmitters, which deliver 0.5 W of continuous power to two inverted-V antennas aligned northwest to southeast. The transmitters operate at 2.72 and 3.64 MHz. Each emits a unique pseudorandom binary phase code (PRN) with a compression ratio of 10,000. The code gain is subsequently increased to a factor of 1E6 in each Doppler bin through coherent signal processing.

Each beacon receiver is a single receiver able to receive signals at two frequencies simultaneously. The receivers use broadband dipole antennas connnected via low-noise amplifiers. Two receivers are deployed at Huancayo and Jicamarca. At both sites, one receiving antenna is aligned northeast to southwest and the other northwest to southeast. The antennas are spatially offset, making it possible to measure both polarization and arrival angle (using interferometry).

Receivers sample at a rate of 10 MS/s at an frequency intermediate between 2.72 and 3.64 MHz. The output is then resampled at 1 MS/s. The effective sample rate is further reduced to 100 kS/s through decimation, yielding a range resolution of 1.5 km. Each range gate is sampled every 100 ms and coherently processed for 10 s. The signal is then detected. Finally, spectra and cross spectra are incoherently integrated for 1 min.

PRN coding makes it possible to measure the group delay or pseudorange, which is a measure of the time of flight of the signals. Formally, the pseudorange is defined as

$$L \equiv \int \frac{c}{v_g}\, \mathrm{d}s = \int \frac{\mathrm{d}}{\mathrm{d}\omega}(\omega n)\, \mathrm{d}s$$

where $n(\omega; k, \cdots)$ is the real part of the index of refraction for the given propagating wave mode which is taken here to be positive, v_g is the group speed, c is the speed of light in vacuum, $\omega = 2\pi f$ is the angular frequency, and ds is an element along a raypath. The Doppler shift of the signal is meanwhile the negative of the time derivative of the optical path length, which is defined as

$$l \equiv \int n\, \mathrm{d}s$$

which is proportional to the physical length of the ray measured in wavelengths. By integrating the negative of the Doppler shift in time, it is possible to estimate the optical path length to within an additive constant.

It is illustrative to contrast the observables in an HF beacon experiment with comparable parameters derived from Global Positioning System signals. Since L-band frequencies are much larger than any of the characteristic frequencies of ionospheric plasmas, the index of refraction can be approximated by the formula $n^2 \approx 1 - 80.48 n_e/f^2$, where n_e is the electron number density such that n itself is always only slightly smaller than unity, viz., $n \sim 1 - \epsilon$ with ϵ proportional to n_e. In this limiting case, we can write

$$L \approx \int (1 + \epsilon)\, \mathrm{d}s$$
$$l \approx \int (1 - \epsilon)\, \mathrm{d}s$$

so that both the pseudorange and the optical path length deviate from the raypath length in proportion to the total electron density. The observables are essentially equivalent in terms of what they indicate about ionospheric structure. Measuring both is desirable in the context of Global Positioning System mainly because of differences in accuracy, precision, and bias.

In the case of HF beacon data, however, the index of refraction is a function of electron density, magnetic field intensity, magnetic aspect angle, electron-neutral collision frequency, and wave frequency given by the Booker quartic or the Appleton-Hartree equation (e.g., Budden, 1985):

$$n^2(\omega, \theta) = 1 - \frac{X}{1 - iZ - \frac{Y^2 \sin^2\theta}{2(1-X-iZ)} \pm \sqrt{\frac{Y^4 \sin^4\theta}{4(1-X-iZ)^2} + Y^2 \cos^2\theta}} \quad (1)$$

(where $X \equiv \omega_p^2/\omega^2$, $Y \equiv \Omega/\omega$, and $Z \equiv \nu/\omega$, where the plus and minus signs correspond to the O and X modes, respectively, and where $\omega = 2\pi f$, ω_p, Ω, and ν are the wave, plasma, electron gyro, and electron-neutral collision frequencies, respectively. The angle θ is the angle between the wave vector and the background geomagnetic field.) The pseudorange and optical path length consequently represent very different moments of the ionospheric electron density. Measuring both independently is advantageous for ionospheric specification. Faraday rotation measurements could provide a third distinct moment in future experimental configurations.

At each time step, the beacon data analysis algorithm determines the first range gate corresponding to the first-hop echo. This is interpreted as the pseudorange of the X-mode signal. The first moment of the Doppler spectrum in the given range gate is then interpreted as the Doppler shift. Presently, only the X-mode pseudorange and the Doppler shift are utilized for analysis. In the future, it should also be possible to make use amplitude, arrival angle, and polarization, all quantities predicted during analysis, although that information is currently being neglected. Likewise, only the first-hop signal is considered presently although data from multiple hops could equally well be incorporated in the data inversion, albeit at increased computational cost and with choices to be made regarding how ground reflection or scatter should be treated.

The pseudorange and Doppler shift for each of the transmitter-receiver links and each frequency are used to estimate the ionospheric electron density in the vicinity of Jicamarca. The inversion process involves three

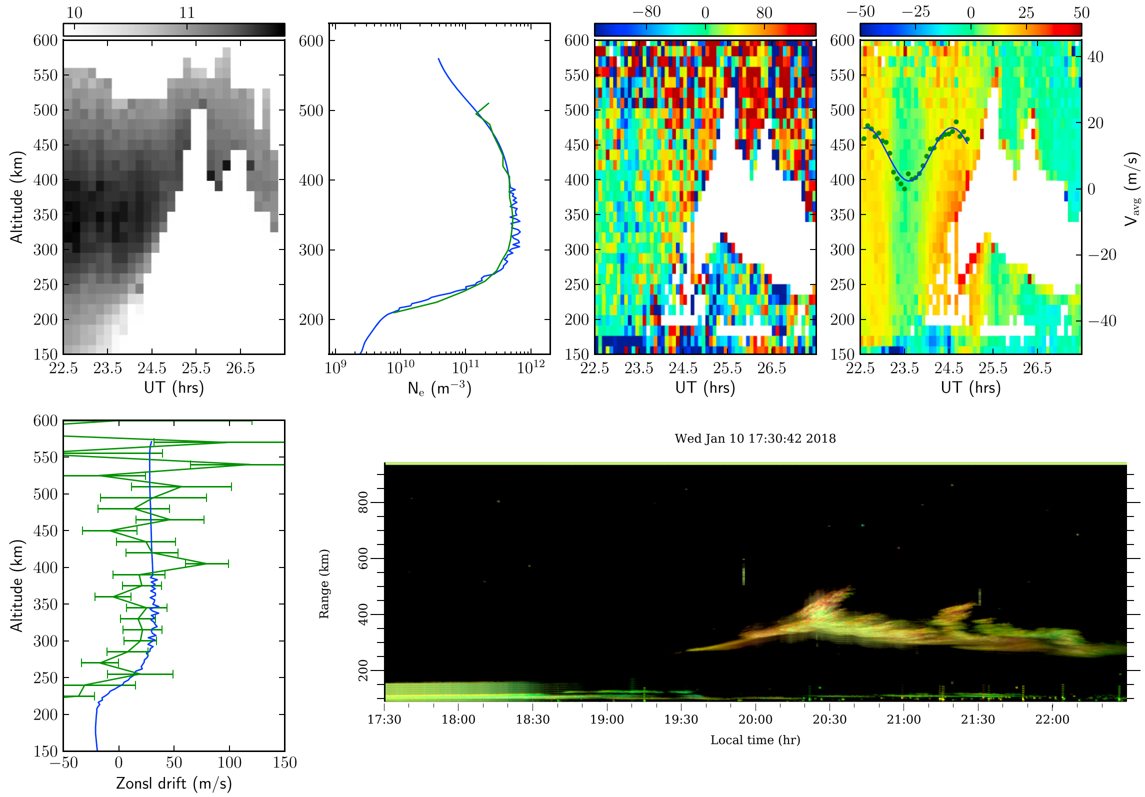

Figure 2. Jicamarca observations for 10 January 2018. (top row, from left to right) Electron density, electron density profiles at 2400 UT (green line) together with computed density profile (blue line), zonal plasma drifts, and vertical plasma drifts. Altitude-averaged vertical drifts are shown by green plotter symbols, with the blue curve representing a fit to the data. (bottom row left) Measured zonal plasma drift profiles at 2400 UT (green line with error bars) together with a computed drift profile (blue line). (bottom row right) Coherent backscatter. Note that UT = LT + 5 hr.

steps or loops. In the inner loop, rays are traced from a given transmitting station using the equations of Hamiltonian optics, which follow directly from Fermat's principle (Holm, 2011). Our algorithm makes use of the formalism given by Jones and Stephenson (1975). We have implemented a high-order Adams multistep method to carry out the ray tracing (Shampine & Gordon, 1975). The magnetic field used to compute the index of refraction is taken from the International Geomagnetic Reference Field (Thébault et al., 2015). The initial azimuth and elevation of the ray are specified, and the ray is traced through a parametrized ionosphere until it returns to the ground. In the middle loop, the azimuth and elevation are varied until the ray returns to the ground at the location of a given receiving station. This is effectively a shooting method for boundary value problems (Press et al., 1988). For each ray, the pseudorange and the optical path length are calculated. The Doppler shift is calculated from the negative of the time derivative of the latter. In practice, time derivatives are computed using backward differencing.

The outer loop involves updating the ionospheric parametrization to optimize the congruity between the predicted and measured pseudorange and Doppler shift observables. The ionosphere is parametrized in the vertical as a three-parameter Chapman function and in the horizontal as an expansion of bicubic B-splines (De-Boor, 1978). The present parametrization employs 15 B-spline coefficients in the zonal direction and 15 in the meridional direction. In total, the regional ionosphere is parametrized using 675 coefficients. This figure is arbitrary.

Additional observables for the ionospheric reconstruction are derived from electron density profiles measured by the Jicamarca ISR directly overhead. Discrepancies between the measured and modeled profile at Jicamarca's latitude and longitude contribute to the objective function used for reconstruction. In practice, initial guess for the ionospheric reconstruction is horizontally homogeneous and nearly matches the initial ISR density profile.

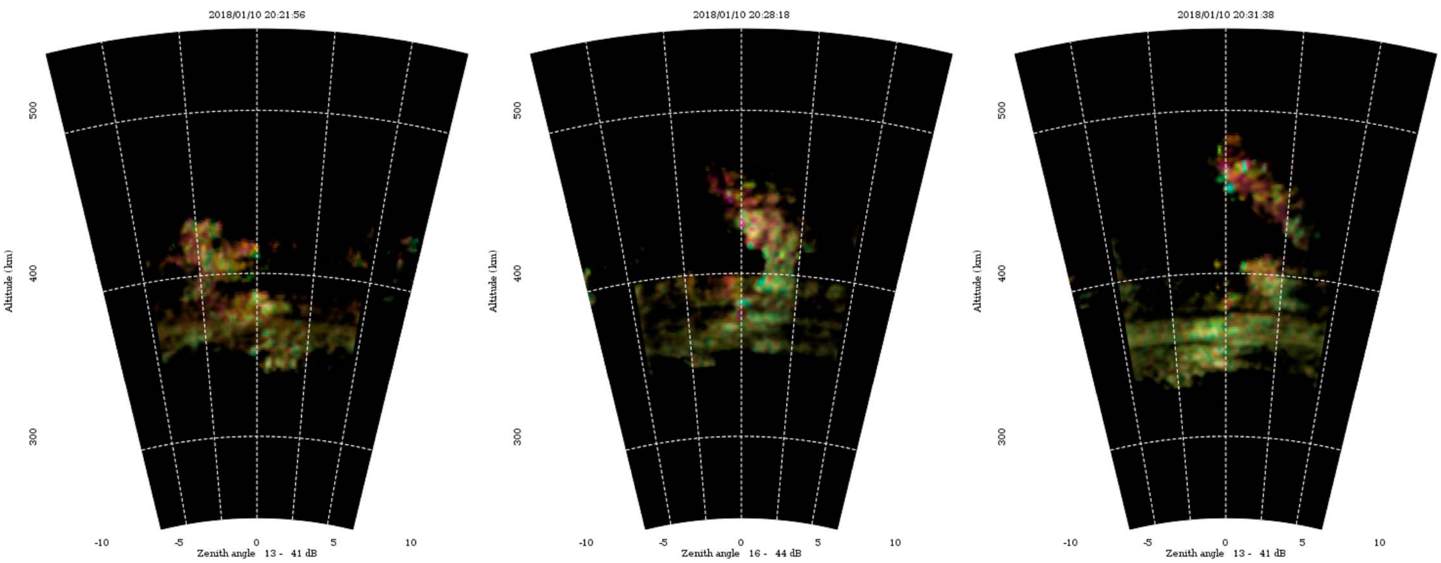

Figure 3. In-beam radar images of the first radar plume observed on 10 January 2018. The images depict the backscatter as functions of range and bearing during short snapshots. The intensity, hue, and saturation of the image pixels convey information about the backscatter signal-to-noise ratio, Doppler shift, and spectral width, respectively. The images show the motion and evolution of the plume over a period of about 10 min.

Optimization is performed using a Levenberg-Marquardt algorithm. Since the reconstruction problem is underdetermined, the algorithm is augmented with the inclusion of second-order Tikhonov regularization, which minimizes the weighted sum of the global curvature of the model ionosphere and the chi-square parameter (see, e.g., Hansen, 2010). Ray tracing continues until the model ionosphere is consistent with the available data. The current solution is used as the initial guess for subsequent time steps. Solutions are formed at 1-min intervals. Additional information about the algorithm and the underlying ionospheric model were given by Hysell et al. (2016).

3. Jicamarca Data

We examine campaign data from 10 and 11 January 2018. Ionospheric irregularities related to ESF formed on the 10th but not on the 11th. Jicamarca observations for January 10 are shown in Figure 2. The top row of the figure shows, from left to right, electron density versus altitude and time, an electron density profile at 2400 UT, zonal plasma drifts versus altitude and time, and vertical plasma drifts versus altitude and time. (These parameters were estimated using a specialized incoherent scatter mode at Jicamarca that measures vertical and zonal plasma drifts, plasma number density, electron and ion temperature, and ion composition simultaneously. The mode subdivides the main antenna array at Jicamarca into subarrays and relies on time division multiplexing. The accuracy of the measurements is somewhat compromised as a result.) The bottom row shows a zonal plasma drift profile at 2400 UT in the left panel. The right panel depicts coherent scatter from 3-m plasma density irregularities, which are telltale of instability. Coherent scatter is much stronger than and obscures incoherent scatter, making plasma parameter estimation impossible in the affected altitudes and times.

The event in question is not a likely candidate for topside ESF. The zonal plasma drifts are modest (uniformly less than about 50 m/s at 2400 UT) and suggestive of relatively weak zonal thermospheric winds. The vertical plasma drifts are also modest, the prereversal enhancement reaching no more than about 20 m/s at its peak at about 2430 UT. The main drivers of the collisional interchange instability are therefore weak. The peak plasma density is also low (less than 5×10^{11} m^{-3} at 2400 UT), a consequence of the 10.7-cm solar flux index being only about 70, and the *F* layer is neither elevated nor rising at the time when ESF is most likely to occur. The bottomside *F* region density gradient is, however, relatively steep.

Nevertheless, the coherent scatter observations show that the *F* region became unstable and produced intense plasma density irregularities, first in the valley region and then in the bottomside. Eventually, several topside plumes were detected, reaching altitudes of about 500 km. This is a marginal example of topside ESF but one that could likely have interfered with transionospheric radio communications.

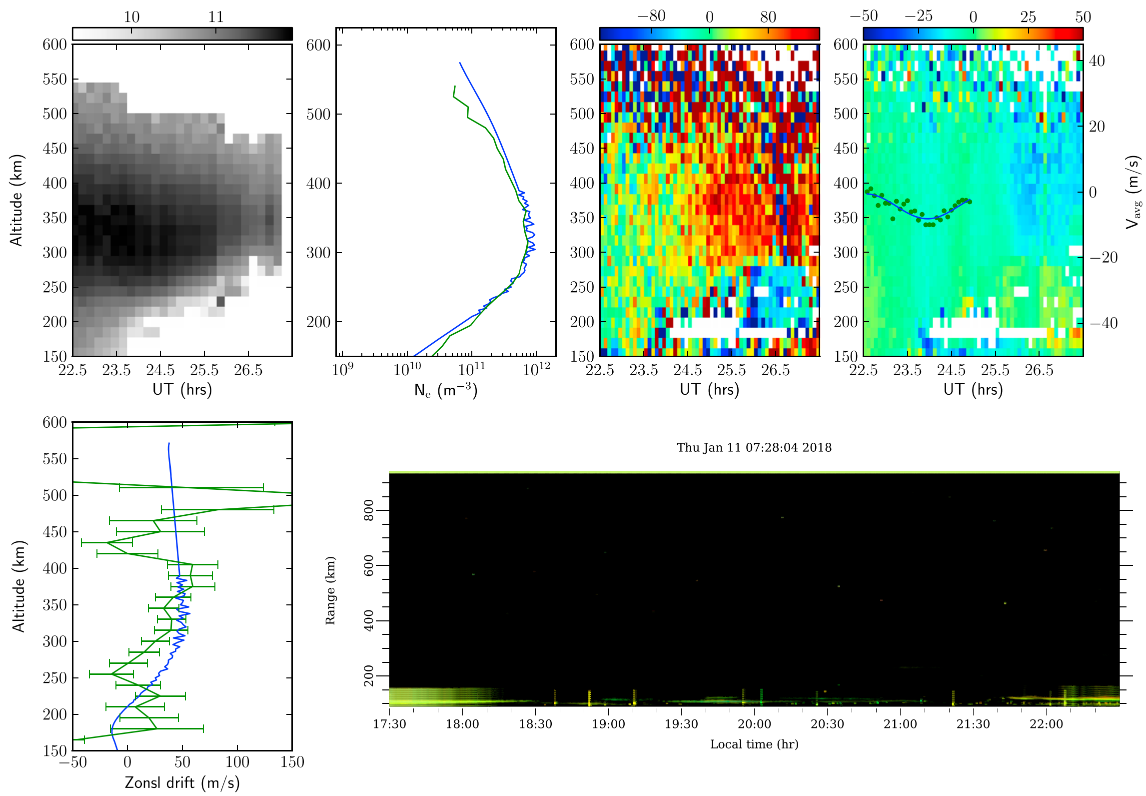

Figure 4. Same as Figure 2 except for 11 January 2018. The plasma density and zonal drift profiles represent conditions at 2330 UT. Note that UT = LT + 5 hr.

A more incisive view of the radar plumes observed on 10 January 2018 is afforded by the application of spaced-antenna methods and aperture synthesis analysis to the coherent scatter data. The techniques determines the spatial distribution of scatterers within the transmitter beam. (For radar imaging purposes, a transmitting antenna module with a half-power full beamwidth of about 6° is employed.) Figure 3 shows images of the earliest plume detected computed at three times spanning the interval when the plume was contained within the radar beam. The images show that the plume was developing rapidly during the time it traversed the radar beam. Having barely emerged from a bottomside layer by about 2020 LT, the plume had penetrated into the topside a mere 10 min later. The morphology of the plume, which is typical of the events observed in this way, can be used to validate the numerical simulations discussed in the next section.

In contrast, Figure 4 shows Jicamarca observations for 11 January 2018, when no ESF irregularities were observed. By comparison to the 10 January event, this one is characterized by slightly denser ionization at the *F* region peak and by stronger zonal plasma drifts, which also exhibit shear flow in the bottomside more distinctly. The plasma density gradient in the bottomside *F* region is shallower, however. Most importantly, there is almost no prereversal enhancement in the vertical plasma drift, which is slightly downward throughout the postsunset period. The 11 January event is superficially therefore even less auspicious for topside ESF than the 10 January event.

The coherent scatter observations show that no irregularities were produced on 11 January. The complete absence of postsunset *F* region irregularities is unusual at all solar flux levels and in all seasons except June solstice at Jicamarca (Fejer et al., 1999). The 10 and 11 January data sets, which were produced under comparable solar and geomagnetic conditions, therefore provide a clear contrast that invites further study.

4. Numerical Simulations

The likelihood of occurrence of ESF can be examined more quantitatively by simulating the collisional interchange instability numerically. The simulation code we use is a fluid simulation, which solves for the electrostatic potential and ion composition in a three-dimensional volume encompassing the equatorial ionosphere in the Peruvian sector. The horizontal neutral wind and the background zonal electric field are specified

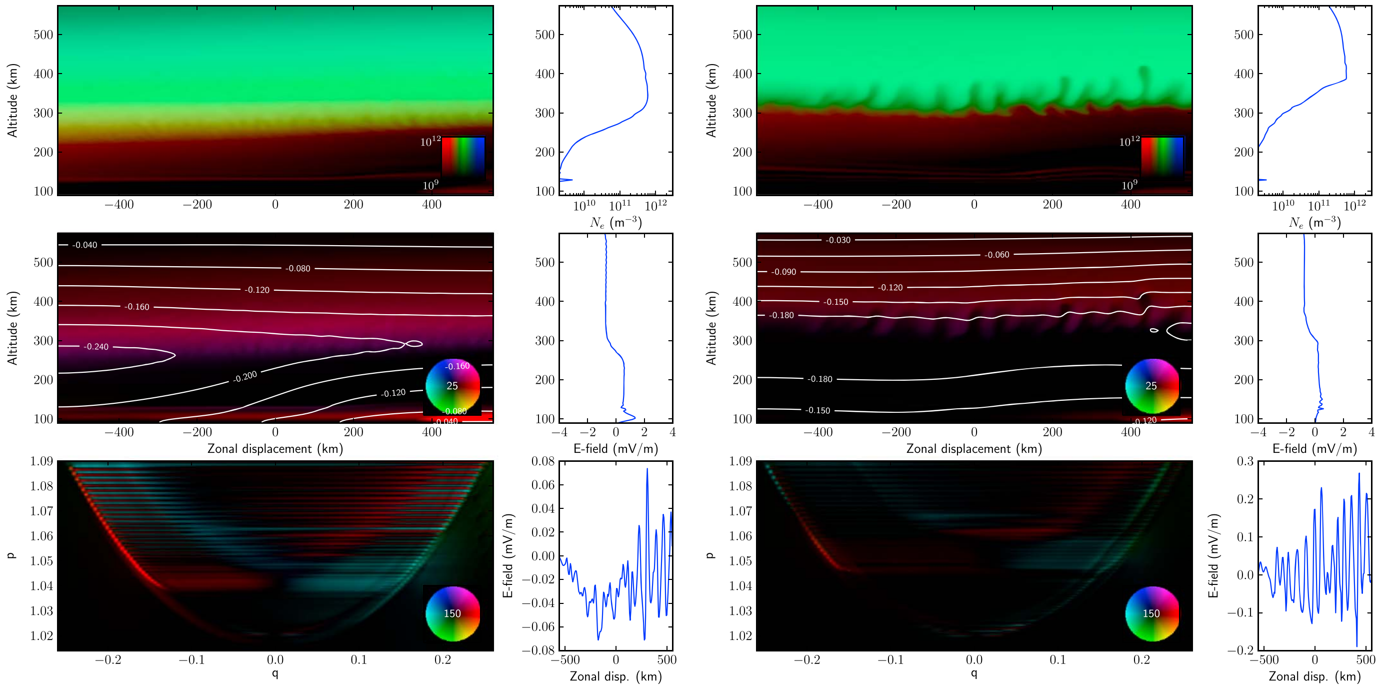

Figure 5. Numerical simulation of the 10 January 2018, equatorial ionosphere over Jicamarca. Figures at left and right depict conditions 30 and 90 min after a simulation start time of 2400 UT, respectively. (top left panels) Ion number density. Red, green, and blue hues represent molecular ions, atomic ions, and hydrogen ions, respectively. (top right panels) Electron number density profiles through the geometric center of the simulation volume. (middle left panels) Current density in the equatorial plane with equipotentials superimposed. (middle right panels) Vertical electric field profile. (bottom left panels) Current density in the meridional plane. (bottom right panels) Zonal electric field along cut through geometric center of simulation.

continuously (together with gravity) as drivers for the simulation. In the inertialess limit, the ion and electron momentum equations can be solved explicitly. The simulation finds the potential by solving the quasineutrality condition in a dipole magnetic coordinate system using a preconditioned stabilized biconjugate gradient method with generalized mixed (Robin) boundary conditions. It then updates the number density of four ion species (O^+, NO^+, O_2^+, and H^+) plus electrons by solving the continuity equation for each species. Charge exchange and dissociative recombination chemistry is included although photo production is not in our postsunset model.

A flux assignment scheme based on the total variation diminishing condition is used to evaluate the convective derivative in the ion continuity equation (Harten, 1983; Trac & Pen, 2003). We use a second-order total variation diminishing scheme with flux limiting (e.g., Van-Leer, 1974) formulated as a MUSCL (monotone upwind schemes for conservation laws). The approach minimizes diffusion and dispersion in the time advance. The method is extended to 3-D using a dimensional splitting technique (Strang, 1968). Time advance is via a second-order Runge-Kutta scheme. Neutral atmospheric parameters are imported from the NRLMSISE-00 model (Picone et al., 2002). The initial ion composition is taken from the IRI-2007 model (Bilitza & Reinisch, 2008). More detailed descriptions of the numerical methods involved were given by Hysell, Jafari, et al. (2014), Hysell, Milla, et al. (2014), and Hysell et al. (2015).

The initial 3-D plasma number density is interpolated from a run of the SAMI2 model, which computes ionospheric state parameters as functions of altitude, latitude, and local time (Huba et al., 2000). For interpolation, we equate local time with longitude here. The solar flux and background electric field parameters used in SAMI2 are scaled to achieve the best overall congruence with electron density profiles measured over Jicamarca at a specified time, which will be the start time of the simulation.

Subsequently, forcing is imposed on the simulation through horizontal neutral winds and background zonal electric field specifications. We import winds from the horizontal wind model (Drob et al., 2015). The winds are scaled to achieve the best congruity between measured and predicted zonal plasma drifts at the start of the simulation. We have found that the modeled plasma drifts resulting from the horizontal wind model winds are generally very similar to the measured zonal plasma drifts given scale factors close to unity. To specify

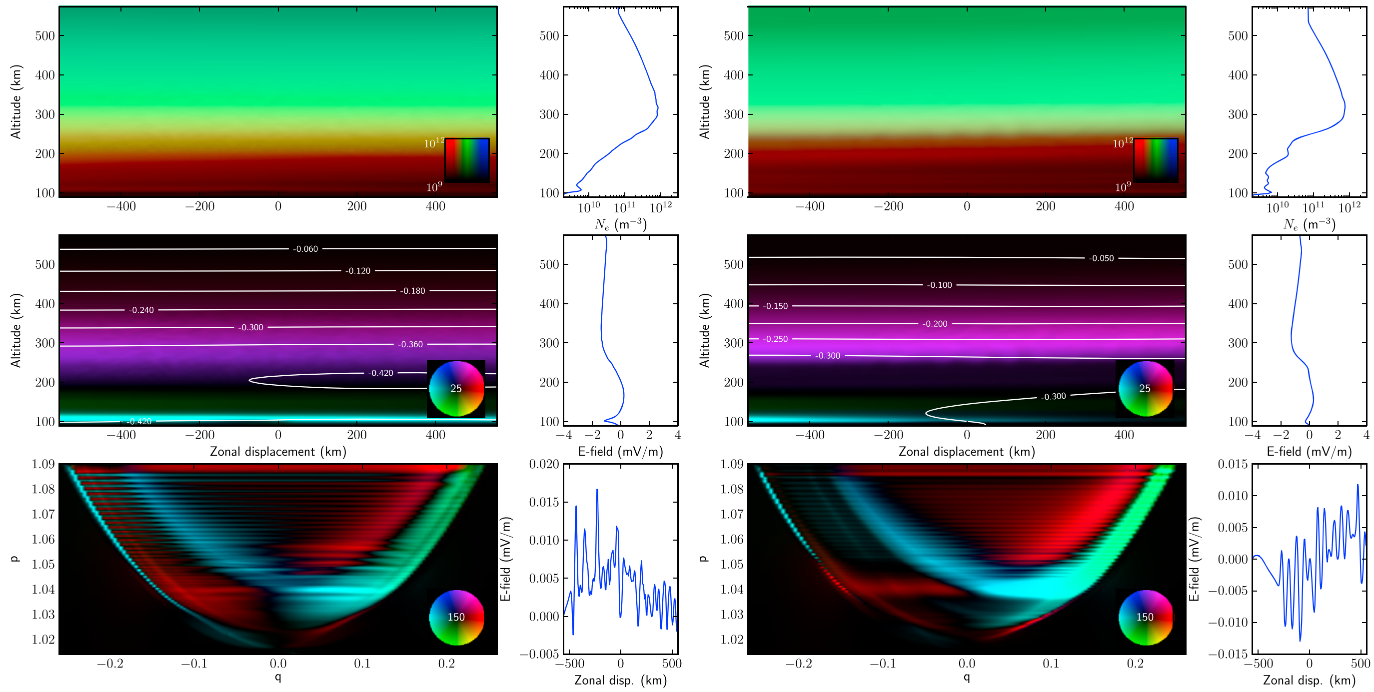

Figure 6. Numerical simulation of the 11 January 2018 equatorial ionosphere over Jicamarca. Figures at left and right depict conditions 30 and 90 min after a simulation start time of 2330 UT, respectively.

the background zonal electric field, we fit a simple functional model to the measured vertical drifts shown in Figure 2. Longitude and local time are equated once again here.

Results of a simulation of the 10 January 2018 event are shown in Figure 5. The simulation was initialized at 2400 UT in the Peruvian sector. Throughout this simulation, both the horizontal neutral winds and the background zonal electric field are modest. Current density in the zonal and meridional planes consequently remains small compared to the other simulations we have documented. The strongest currents in the equatorial plane are in the vertical direction and arise from an inefficient *F* region dynamo and differential plasma and neutral horizontal motions. A vortex is evident after 30 min when bottom-type plasma density irregularities excited by vertical currents can be seen to be forming at the base of the bottomside. After 90 min, normal collisional interchange instability is underway, with bottomside irregularities predominating between 300- and 400-km altitude. At these altitudes, currents due to gravity are still small, and zonal Pedersen currents driven by the background electric field are also small. The bottomside irregularities therefore have not developed into major plumes although one or two have just managed to enter the topside. The resemblance between the simulated depletions and the images in Figure 3 is fairly close except for the crucial fact that the depletions in simulation never show the kind of rapid development seen in the images. This is a case of missed detection.

Figure 6 shows results for the 11 January event. In this case, the horizontal neutral winds are much stronger than in the 10 January case, and the current densities are consequently stronger. The shallow bottomside density profile means that conductivity is distributed over a broader range of altitudes than on 10 January, and competing neutral wind dynamos in different altitude strata drives strong field-aligned currents throughout the region. However, the westward background electric field that exists throughout the simulation is highly stabilizing, and irregularities never form—even in the valley region. The simulation therefore correctly predicts the complete absence of irregularities, bottom-type, bottomside, or topside, on 11 January.

5. Beacon Data

To investigate the missed detection, we turn to data from the HF beacon network for wider regional specifications of the ionosphere during the two events in question. Figure 7 shows pseudorange data for four raypaths and two frequencies (i.e., eight rays total) for 10 and 11 January 2018, from 1800 to 2100 LT. Only the first hop is considered in each case. Prior to 1800 LT, absorption typically renders reception unreliable. Data

10.1029/2018JA025648

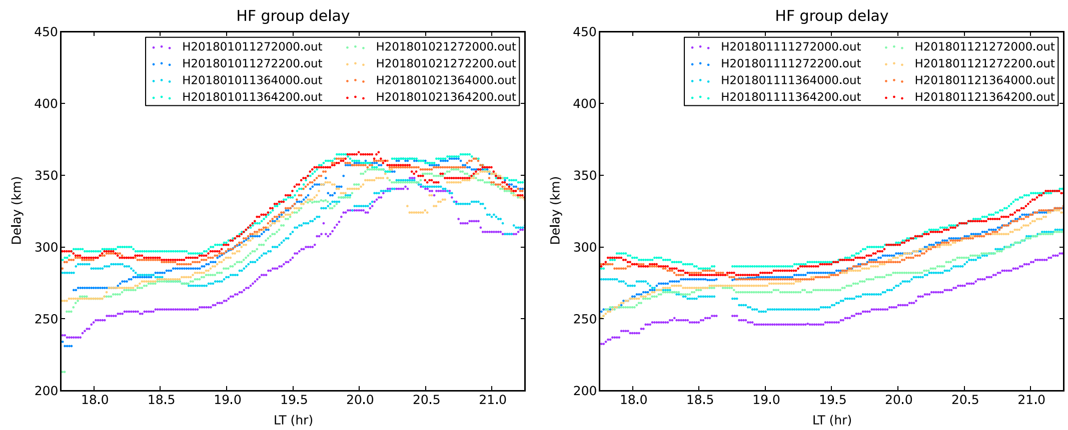

Figure 7. Pseudorange measurements for (left) 10 January and (right) 11 January, 2018. The convention is to plot half the pseudorange, a quantity more closely comparable to altitude. Raypaths are designated by names of the form Hyyyydddrrffft00.dat where yyyy is year, ddd is day number, rr is receiver, fff is frequency, and t is transmitter. The receiver options are 11 for Jicamarca and 21 for Huancayo. (We presently consider results for only one of the two receivers located at each site.) The transmitter options are 0 for Ancon and 2 for Ica. HF = high frequency.

between midnight and sunrise typically look similar to the curves shown here only with the altitude trend being reversed in time.

The pseudorange measurements are generally increasing functions of time during the periods in question, although some wavelike behavior is sometimes also evident, particularly late in the 10 January event when the measurements reach a plateau. Different raypaths exhibit wavelike variations at different times. The Ica raypaths, which are the longest, are the most variable, particularly the Ica-Huancayo paths. The pseudoranges increased more rapidly with time on 10 January than 11 January. While this is consistent with the ISR drifts data in Figures 2 and 4, the pseudorange is obviously a poor proxy for and should not be regarded as a measurement of the proper vertical motion of the ionospheric medium (whereas incoherent scatter does measure proper motion). Proper vertical motion in this case is evidently not even the dominant factor in the time rate of change of the pseudorange, which is influenced by changes due to chemistry and advection. Similar remarks hold for the optical path length observable, which is considered below. For a detailed investigation of the factors that control the Doppler shift of HF signals, see Bennett (1972). For clear examples of the distinction between HF Doppler measurements and the proper motion of the ionosphere, see Woodman et al. (2006).

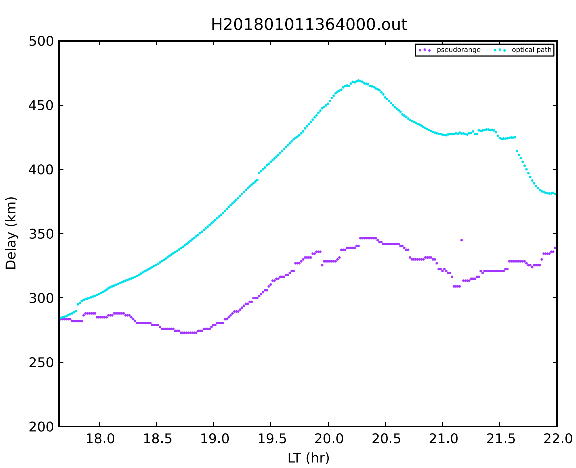

Figure 8. Comparison between pseudorange (violet) and optical path length (cyan) for the 3.64-MHz raypath between Ancon and Jicamarca on 10 January 2018. The vertical offset of the optical raypath measurement, which is derived by integrating the negative of the Doppler shift, is arbitrary. By convention, both quantities were divided by 2 for plotting.

The difference between the pseudorange and the optical raypath is illustrated by Figure 8. In some cases, the two observables are similar. In this example, however, the two curves are quite dissimilar in their details, even exhibiting different signs at times. Still greater differences exist in some cases. We point this out just to highlight the fact that the two observables give independent information about the ionosphere.

Ionospheric reconstructions based on HF beacon and Jicamarca ISR data are shown in Figures 9 and 10 for 10 and 11 January 2018, respectively. The figures have six panels, each representing six different local times. (Recall that reconstructions are computed at a cadence of once per minute.) Each panel shows two rays for two frequencies bridging the four transmitter-receiver permutations possible in the network. Also shown is a parametrized electron density profile at the latitude and longitude of Jicamarca. Isodensity contours for $N_e = 5 \times 10^{10}$ m^{-3} (green) and 3.5×10^{11} m^{-3} (cyan) are superimposed. Note that the isodensity contour heights are scaled to emphasize horizontal gradients.

At 1800 LT, the data were consistent with a horizontally uniform ionosphere. The HF rays propagated along great-circle paths, and the ray pairs were each coplanar. Between 1800 and 1900 LT, the bottomside steepened under the influence of chemical recombination. Steepening proceeded

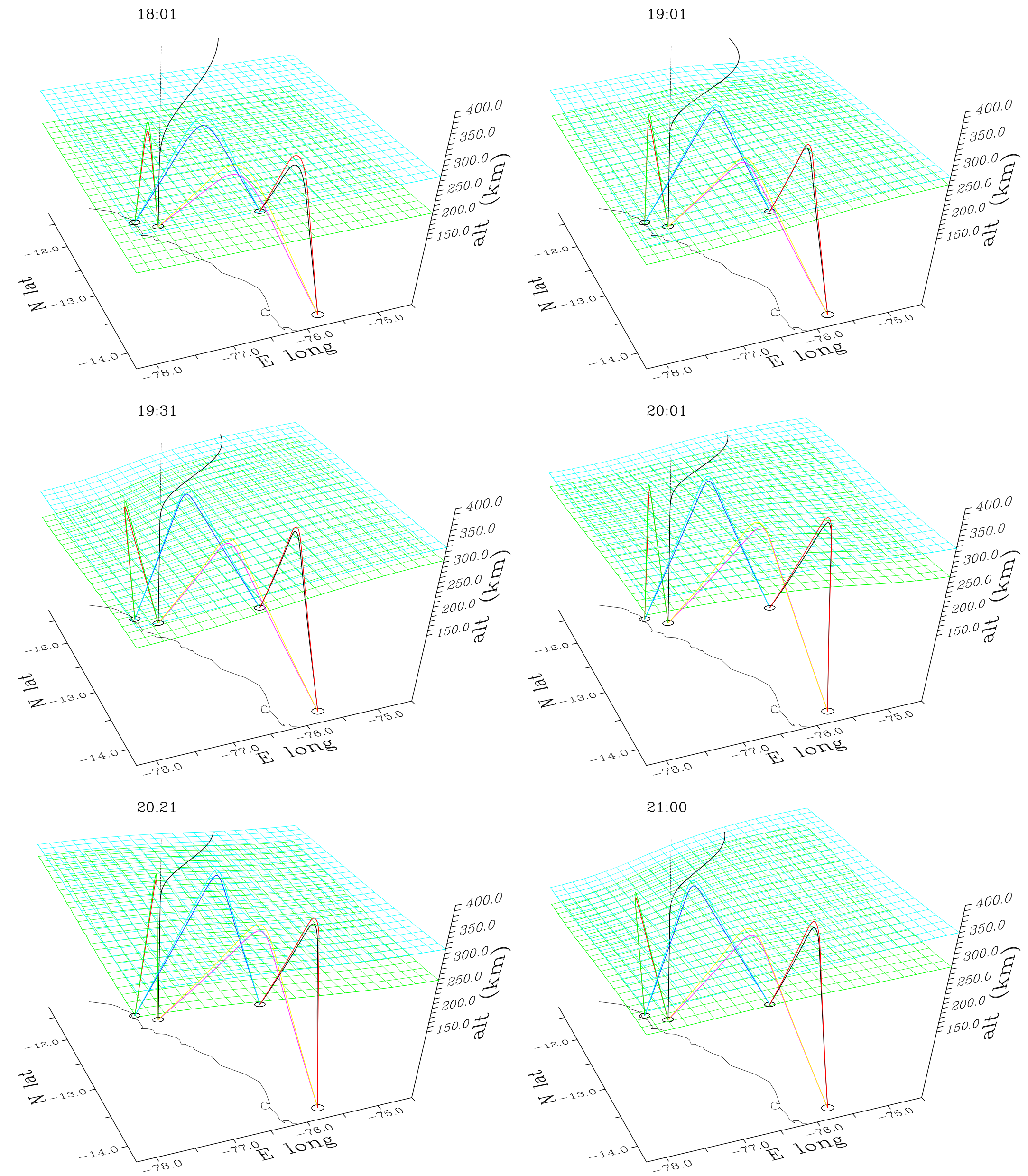

Figure 9. Ionospheric reconstruction for 10 January 2018. Rays connect high-frequency transmission and reception sites. A parametrized electron density profile is shown at the latitude and longitude of the Jicamarca Radio Observatory. Isodensity contours depict electron densities of 5 $\times 10^{10}$ m^{-3} (green) and 3.5 $\times 10^{11}$ m^{-3} (cyan). The curves are plotted so as to accentuate gradients, with departures from the mean contour height scaled by a factor of 3.

from east to west with the motion of the solar terminator. The steep bottomside caused the pseudoranges for the ray pairs to be similar despite the HF frequencies being different. By 1900 LT, the ionosphere was again nearly level and uniform across the region.

Between 1900 and 2000 LT, the ionosphere ascended in an action that also swept from east to west with time. The zonal gradient in layer height was most evident at about 1930 LT. The gradient was accompanied by HF rays propagating outside great-circle paths and by noncoplanar ray pairs. By 2000 LT, the western edge had caught up with the eastern edge, and the ionosphere was again nearly level. The event coincided with the passage of the prereversal enhancement of the zonal electric field, a phenomenon the beacon technique is evidently able to track. Monitoring the prereversal enhancement is critical for ESF forecasting. The HF network may be superior to ISR measurements at Jicamarca in some respects, being more resilient to contamination from plasma density irregularities.

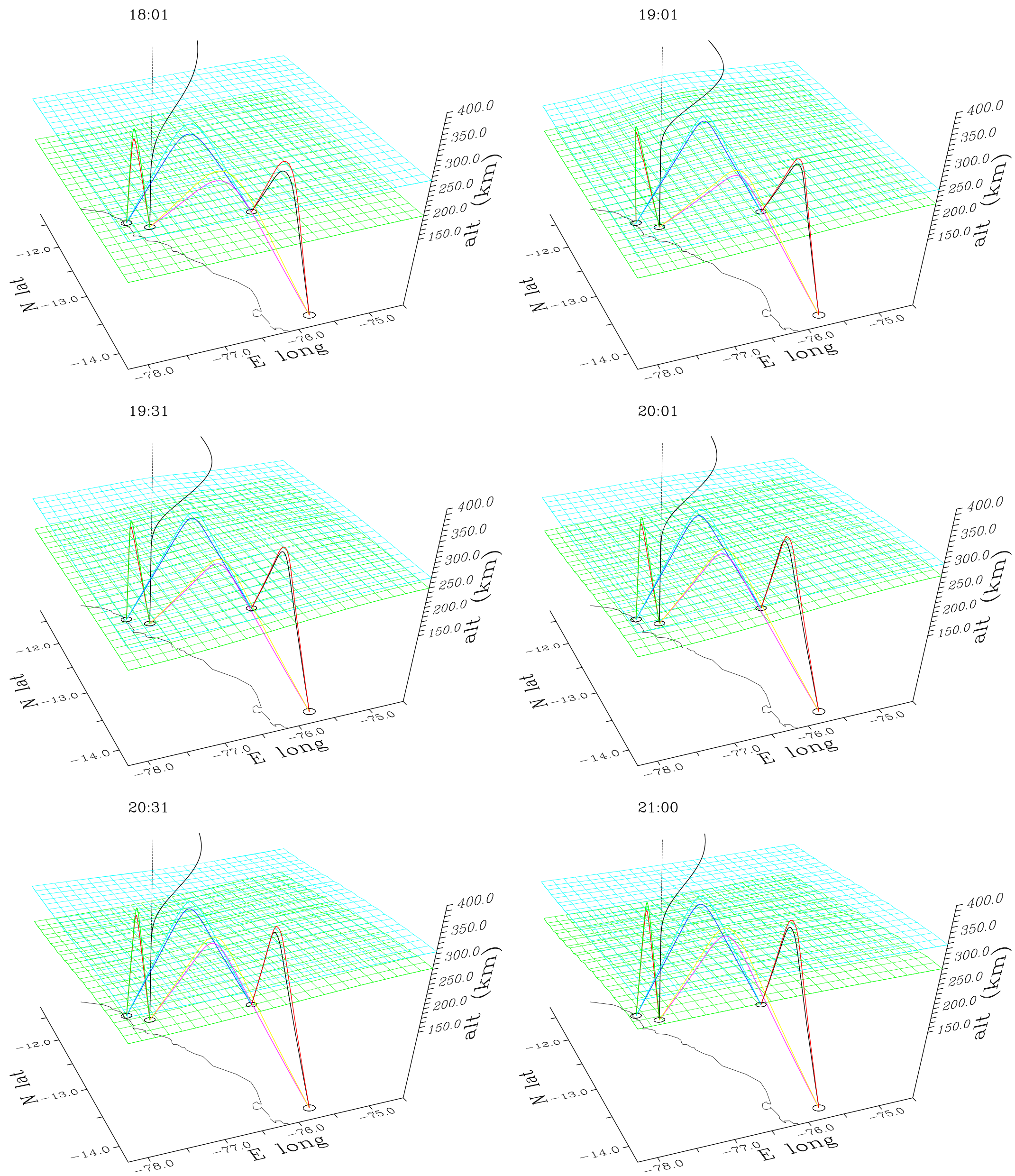

Figure 10. Ionospheric reconstruction for 11 January 2018.

After 2000 LT, however, the western edge of the region resumed its ascent, leading to the tilt in the layer height evident in the reconstruction at 2020 LT. The tilt is significant since it indicates a break in the equivalence of longitude with local time in the background flow. More specifically, it indicates that the postsunset uplift was stronger to the west of Jicamarca's longitude than it was directly overhead. In the reconstruction, the uplift sweeps from west to east, the eastern edge of the region ultimately residing at a higher altitude than the western edge at 2100 LT. As the first radar plume of the evening was emerging at precisely 2020 LT, care must be taken with the interpretation of the reconstructions at later times when changes in layer height are probably better interpreted as effects rather than causes of instability and ionospheric irregularities.

In addition to the aforementioned secular variations, the ionospheric reconstruction also exhibits wavelike and transient variations, although this is not apparent in the fixed frames in Figure 9. These seem to be much less important than the dramatic changes in layer height described above however.

The 11 January 2018, ionospheric reconstruction begins much the same way as the 10 January event. Between 1801 and 1900 LT, the bottomside steepens under the action of recombination in a manner that progresses from east to west albeit to a lessor degree than on the previous evening. However, there is little ionospheric evolution thereafter. Variations in layer height are small, gradual, and uniform. There is no obvious prereversal enhancement. The most significant horizontal gradients in layer height are meridional rather than zonal and may suggest the presence of meridional winds which are generally (but not always) stabilizing (Huba & Krall, 2013).

6. Analysis

The original impetus for the beacon network were a few radar plumes seen over Jicamarca in past campaigns when ionospheric conditions seemed unfavorable. The plumes in question were seen mainly either immediately at sunset, when interchange instabilities should not have had sufficient time to produce well-developed radar plumes, or several hours after sunset, when the background electric field, neutral winds, and bottomside density gradient are typically unfavorable for instability. Milla et al. (2015) speculated that external agents such as medium-scale traveling ionospheric disturbances or fossil plumes drifting in from the day side may have been responsible (see, e.g., Krall et al., 2011).

In the case of the 10 January 2018, modest radar plumes were observed over Jicamarca in the time interval when plumes are most likely and under conditions that were unfovorable but not prohibitive for ESF, including a steep bottomside and a distinct if modest prereversal enhancement. The plumes developed to a greater degree than simulations based on Jicamarca ISR data anticipated, however. We turn to the HF beacon data to understand why.

Experimental results from individual raypaths on 10 and 11 January 2018, as shown in Figure 7, are suggestive. The pseudorange data suggest greater postsunset uplift on 10 January, something which was already obvious in the Jicamarca ISR data. They also suggest more irregular uplift from about 1930 LT onward when quasiperiodic fluctuations are evident in multiple traces. While it is tempting to associate the fluctuating drifts with gravity waves or other candidate ESF trigger agents, we note also that bottomside spread *F* irregularities were present by 1930 LT, and so the fluctuations could be indications of existing plasma waves and instabilities rather than of causes. It is also noteworthy that the fluctuations in the raw pseudorange data tend to diminish in the ionospheric reconstructions (e.g., Figure 9). This is because small layer tilts generally give rise to large deviations in pseudorange as raypaths deviate from great-circle paths. Conversely, small tilts imply large pseudorange fluctuations. We should be reluctant to read much into them, although small, wavelike fluctuations are visible in the full ionospheric reconstructions when viewed completely in animated form (not shown).

The salient features of the 10 and 11 January 2018 events are most apparent in the ionospheric reconstructions (Figures 9 and 10). Both reconstructions show the postsunset steepening of the *F* region bottomside. Only the 10 January event shows steep zonal gradients in layer height. These sweep through the field of view following the timing of the prereversal enhancement seen in the Jicamarca ISR data through about 2000 LT. Crucially, however, the ionosphere on the west side of the reconstruction reached higher altitude than the east side. Longer sustained vertical drifts to the west of Jicamarca, as indicated by the HF beacon data, would have excited more developed interchange instabilities, irregularities, and depletions, which would have drifted eastward and over the observatory at a later time. This could explain how the radar plumes observed on 10 January developed. In this scenario, the background circulation defied the approximation equating longitude and local time. A key assumption in the forecast methodology thus seems to have been violated.

7. Summary

Previous after-the-fact forecast studies using the methodology and the simulation described in this paper successfully reproduced the occurrence or nonoccurrence of interchange instabilities in the F region over Jicamarca during quiet geomagnetic conditions over a variety of seasons and solar flux levels (Hysell, Jafari, et al., 2014; Hysell, Milla, et al., 2014; Hysell et al., 2015). A few missed detections were also documented, including radar plumes observed either too early or too late in the postsunset period to be accounted for by the methodology or by conventional wisdom about the conditions required for ESF. One possibility is that the radar plumes and underlying plasma density depletions were generated under conditions that could not be captured by the Jicamarca ISR looking immediately overhead. Such conditions could include exotic agents like thermospheric gravity waves and medium-scale traveling ionospheric disturbances or tamer factors such as a prereversal enhancement with a peak intensity that varies with longitude.

In this study, small radar plumes were observed in the postsunset sector that were unremarkable except for the fact that they were not anticipated by the numerical simulation. The background ionospheric conditions detected by the Jicamarca ISR did not seem very favorable for the formation of topside plumes. The HF beacon data provided additional information about the spatial configuration of the *F* region and the circulation, namely, that the amplitude of the prereversal enhancement may have been larger to the west of Jicamarca than overhead. A change of even a few meters per second can be enough to make the difference between predicting bottomside spread *F* and radar plumes.

The purpose of the HF beacon network is to expand the coverage of the Jicamarca Radio Observatory and offer a view into the horizontal structure of the regional ionosphere. Although the network is still sparse, the eight paths between the four existing stations give indications about east-west and north-south gradients at different altitudes. The group delay and Doppler shift observables are uniquely informative, being sensitive to different aspects of the configuration of the ionosphere. In the future, it should be possible to expand the network and to measure and utilize other observables for reconstruction, including the arrival angle and the amplitude. Modeling the absorption in particular could provide a view into the equatorial *D* region, which has so far been difficult to probe at Jicamarca. Incorporating data from multiple hops should be possible if computationally expensive. Expanding the HF network in the north-south direction would also provide a view into the strength of the meridional winds and the development of the midlatitude anomalies, critical factors for ESF forecasting.

Acknowledgments
This work was supported by award FA9550-12-1-0462 from the Air Force Office of Scientific Research to Cornell University. The Jicamarca Radio Observatory is a facility of the Instituto Geofisíco del Perú operated with support from NSF award AGS-1732209 through Cornell. The help of the staff is much appreciated. We also appreciate help with the SAMI2 model received form Joseph Huba at the Naval Research Laboratory. Data used for this publication are available through the Madrigal database.

References

Aveiro, H. C., & Hysell, D. L. (2012). Implications of the equipotential field line approximation for equatorial spread *F* analysis. *Geophysical Research Letters*, *39*, L11106. https://doi.org/10.1029/2012GL051971

Bennett, J. (1972). The ray theory of Doppler frequency shifts. *Australian Journal of Physics*, *21*, 259.

Bilitza, D., & Reinisch, B. W. (2008). International Reference Ionosphere 2007: Improvements and new parameters. *Advances in Space Research*, *42*, 599–609.

Booker, H. G., & Wells, H. W. (1938). Scattering of radio waves by the *F* region. *Terrestrial Magnetism*, *43*, 249–256.

Budden, K. (1985). *The propagation of radio waves*. New York: Cambridge University Press.

Costa, E., & Kelley, M. C. (1978). On the role of steepened structures and drift waves in equatorial spread *F*. *Journal of Geophysical Research*, *83*, 4359–4364.

De-Boor, C. (1978). *Practical Guide to Splines*. New York: Springer Verlag.

Drob, D. P., Emmert, J. T., Meriwether, J. W., Makela, J. J., Doornbos, E., Conde, M., et al. (2015). An update to the horizontal wind model (HWM): The quiet time thermosphere. *Earth and Space Science*, *2*, 301–319. https://doi.org/10.1002/2014EA000,089

Fejer, B. G., Scherliess, L., & de Paula, E. R. (1999). Effects of the vertical plasma drift velocity on the generation and evolution of equatorial spread *F*. *Journal of Geophysical Research*, *104*(19), 19,859–19,869. https://doi.org/10.1029/1999JA900271

Hansen, P. C. (2010). *Discrete Inverse Problems: Insight and Algorithms*. Philadelphia: SIAM.

Harten, A. (1983). High resolution schemes for hyperbolic conservation laws. *Journal of Computational Physics*, *49*, 357–393.

Holm, D. D. (2011). *Geometric Mechanics Part 1: Dynamics and symmetry*. London: Imperial College Press.

Huba, J. D., Joyce, G., & Fedder, J. A. (2000). Sami2 is another model of the ionosphere (SAMI2): A new low-latitude ionospheric model. *Journal of Geophysical Research*, *105*, 23,035–23,054. https://doi.org/10.1029/2000JA000035

Huba, J. D., Joyce, G., & Krall, J. (2008). Three-dimensional equatorial spread *F* modeling. *Geophysical Research Letters*, *35*, L10102. https://doi.org/10.1029/2008GL033,509

Huba, J. D., & Krall, J. (2013). Impact of meridional winds on equatorial spread *F*: Revisited. *Geophysical Research Letters*, *40*, 1268–1272. https://doi.org/10.1002/grl.50,292

Hysell, D. L., Jafari, R., Milla, M. A., & Meriwether, J. W. (2014). Data-driven numerical simulations of equatorial spread *F* in the Peruvian sector. *Journal of Geophysical Research: Space Physics*, *119*, 3815–3827. https://doi.org/10.1002/2014JA019889

Hysell, D. L., & Kudeki, E. (2004). Collisional shear instability in the eqautorial *F* region ionosphere. *Journal of Geophysical Research*, *109*, A11301.

Hysell, D. L., Milla, M. A., Condori, L., & Meriwether, J. W. (2014). Data-driven numerical simulations of equatorial spread *F* in the Peruvian sector: 2. Autumnal equinox. *Journal of Geophysical Research: Space Physics*, *119*, 6981–6993. https://doi.org/10.1002/2014JA020345

Hysell, D. L., Milla, M. A., & Vierinen, J. (2016). A multistatic HF beacon network for ionospheric specification in the Peruvian sector. *Radio Science*, *51*, 392–401. https://doi.org/10.1002/2016RS005951

Jones, R. M., & Stephenson, J. J. (1975). A versatile three-dimensional ray tracing computer program for radio waves in the ionosphere: Technical Report U.S Department of Commerce.

Kelley, M. C., Makela, J. J., de la Beaujardiere, O., & Retterer, J. (2011). Convective ionospheric storms: A review. *Reviews of Geophysics*, *49*, RG2003. https://doi.org/10.1029/2010RG000340

Keskinen, M., & Chaturvedi, P. (1980). Preliminary report of numerical simulations of intermediate wavelength collisional Rayleigh-Taylor Instability in equatorial spread F. *Journal of Geophysical Research*, *85*(A4), 1775–1778. https://doi.org/10.1029/JA085iA04p01775

Krall, J., Huba, J. D., Ossakow, S. L., Joyce, G., Makela, J. J., Miller, E. S., & Kelley, M. C. (2011). Modeling of equatorial plasma bubbles triggered by non-equatorial traveling ionospheric disturbances. *Geophysical Research Letters*, *38*, L08103. https://doi.org/10.1029/2011GL046890

Milla, M. A., Condori, L., & Vierinen, J. (2015). Data-driven numerical simulations of equatorial spread *F* in the Peruvian sector 3: Solstice. *Journal of Geophysical Research: Space Physics*, *120*, 10,809–10,822. https://doi.org/10.1002/2015JA021,877

Ossakow, S. L. (1981). Spread *F* theories—A review. *Journal of Atmospheric and Terrestrial Physics*, *43*, 437.

Picone, J. M., Hedin, A. E., Drob, D. P., & Aikin, A. C. (2002). NRLMSISE-00 Empirical model of the atmosphere: Statistical comparisons and scientific issues. *Journal of Geophysical Research*, *107*, A12. https://doi.org/10.1029/2002JA009430

Press, W. H., Flannery, B. P., Teukolsky, S. A., & Vetterling, W. T. (1988). *Numerical Recipes in C*. New York: Cambridge Univ Press.

Retterer, J. M. (2010). Forecasting low-latitude radio scintillation with 3-D ionospheric plume models: 1. Plume model. *Journal of Geophysical Research*, *115*, A03306. https://doi.org/10.1029/2008JA013839

Shampine, L. F., & Gordon, M. K. (1975). *Computer Solution of Ordinary Differential Equations: The Initial Value Problem*. San Francisco: Freeman and Co.

Strang, G (1968). On the construction and comparison of difference schemes. *SIAM Journal on Numerical Analysis*, *5*, 506–517.

Thébault, E., Finlay, C. C., Beggan, C. D., Alken, P., Aubert, J., et al. (2015). International Geomagnetic Reference Field: The 12th generation. *Earth, Plantes, and Space*, *67*, 79. https://doi.org/10.1186/s40,623-015-0228-9

Trac, H., & Pen, U. L. (2003). A primer on Eulerian computational fluid dynamics for astrophysicists. *Astrophysics*, *115*, 303–321.

Van-Leer, B. (1974). Towards the ultimate conservation difference scheme. II. Monotonicity and conservation combined in a second-order scheme. *Journal of Comparative Physiology*, *14*, 361.

Woodman, R. F. (2009). Spread F—An old equatorial aeronomy problem finally resolved? *Annales de Geophysique*, *27*, 1915–1934.

Woodman, R. F., Chau, J. L., & Ilma, R. R. (2006). Comparison of ionosonde and incoherent scatter drift measurements at the magnetic equator. *Geophysical Research Letters*, *33*, L01103. https://doi.org/10.1029/2005GL023,692

Yokoyama, T., Shinagawa, H., & Jin, H. (2014). Nonlinear growth, bifurcation and pinching of equatorial plasma bubble simulated by three-dimensional high-resolution bubble model. *Journal of Geophysical Research: Space Physics*, *119*, 10,474–10,482.

Zargham, S., & Seyler, C. E. (1987). Collisional interchange instability, 1, Numerical simulations of intermediate-scale irregularities. *Journal of Geophysical Research*, *92*, 10,073.